Supporting Information

Contents

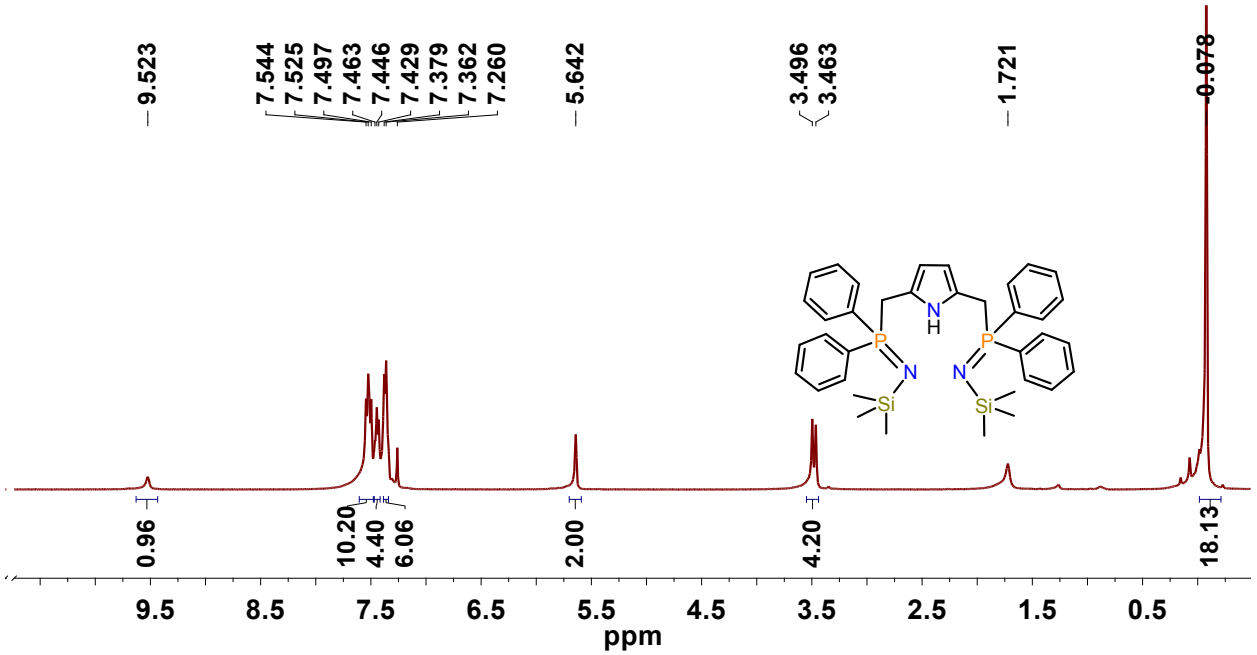

Figure S1. The ^{1}H NMR spectrum (400 MHz, 25 °C) in $CDCl_3$ of 2,5-bis(diphenylphosphinoiminomethyl)pyrrole **2**.

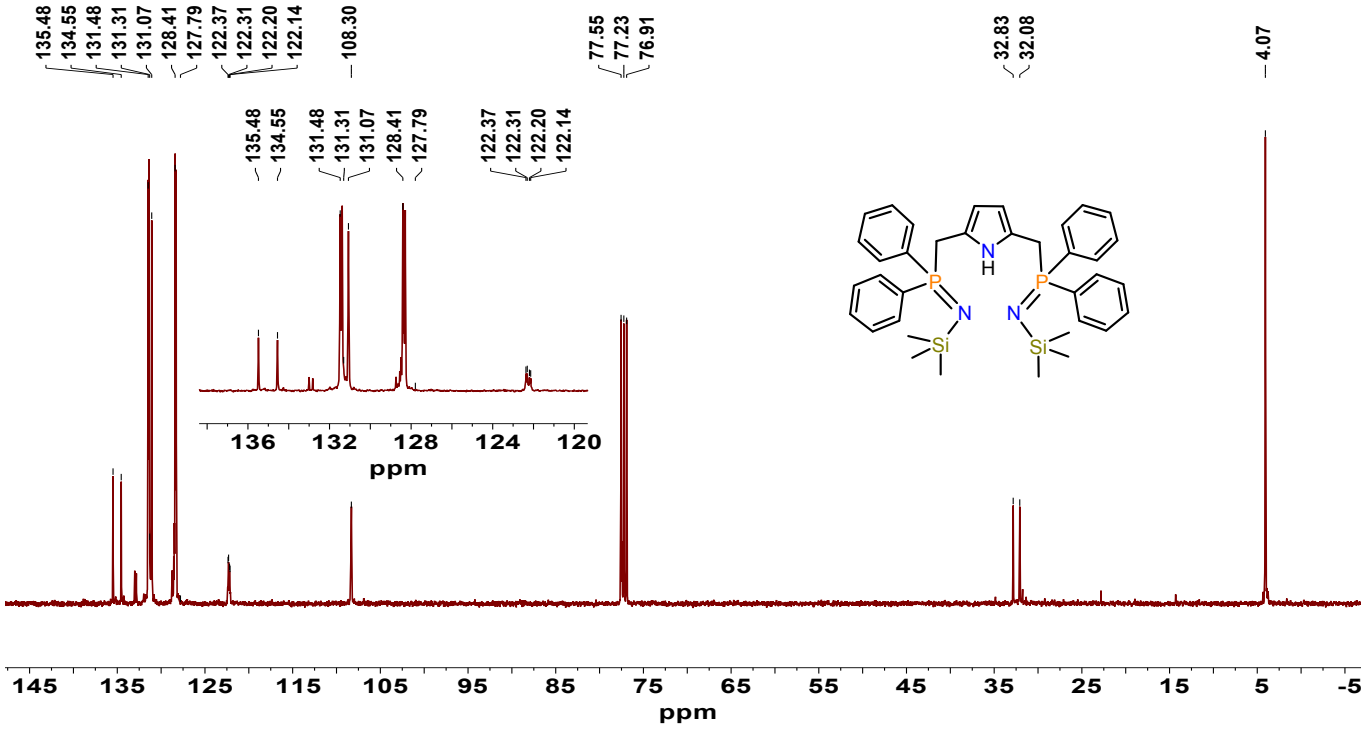

Figure S2. The ^{13}C NMR spectrum (100.6 MHz, 25 °C) in $CDCl_3$ of 2,5-bis(diphenylphosphino iminomethyl)pyrrole **2**.

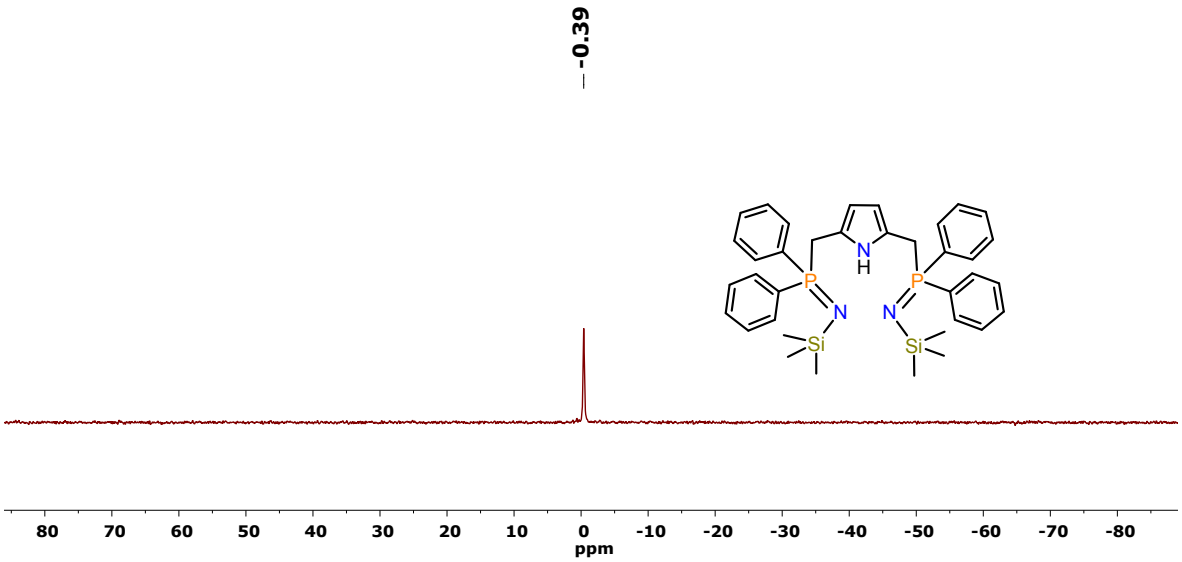

Figure S3. The $^{31}P\{^{1}H\}$ NMR spectrum (161.9 MHz, 25 °C) of **2** in toluene with external D_2O.

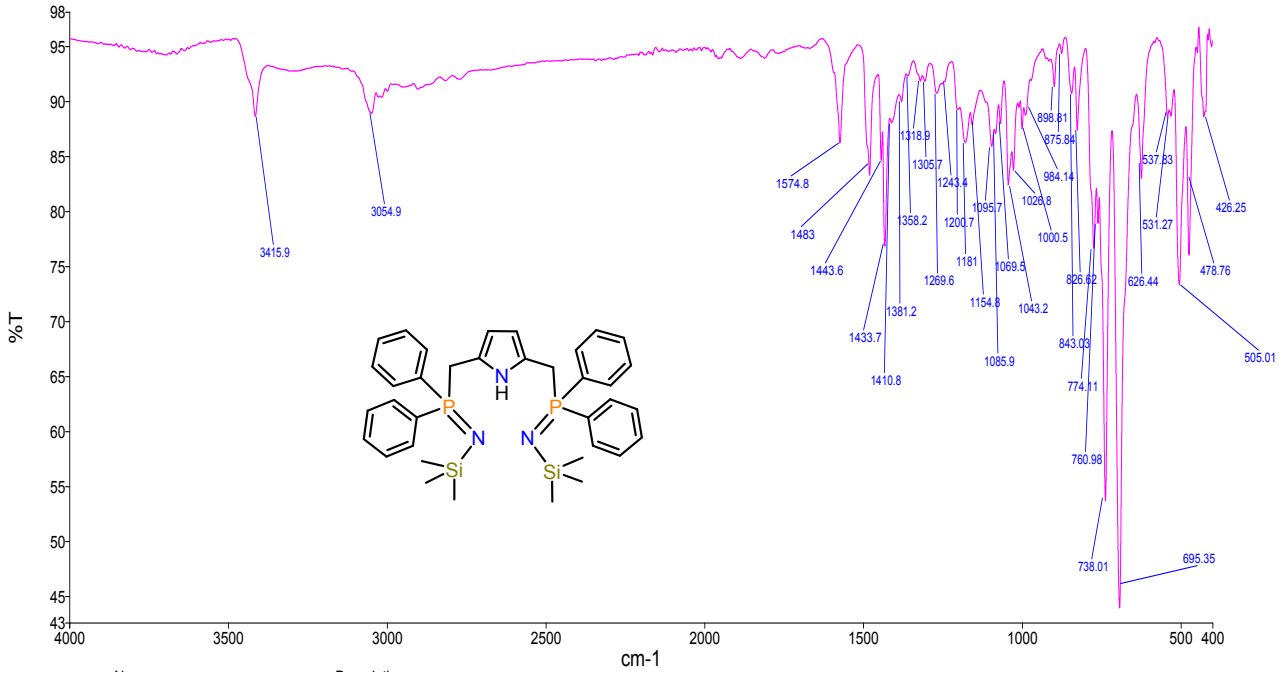

Figure S4. The FTIR spectrum (ATR mode) of 2,5-bis(diphenylphosphinoiminomethyl)pyrrole **2**.

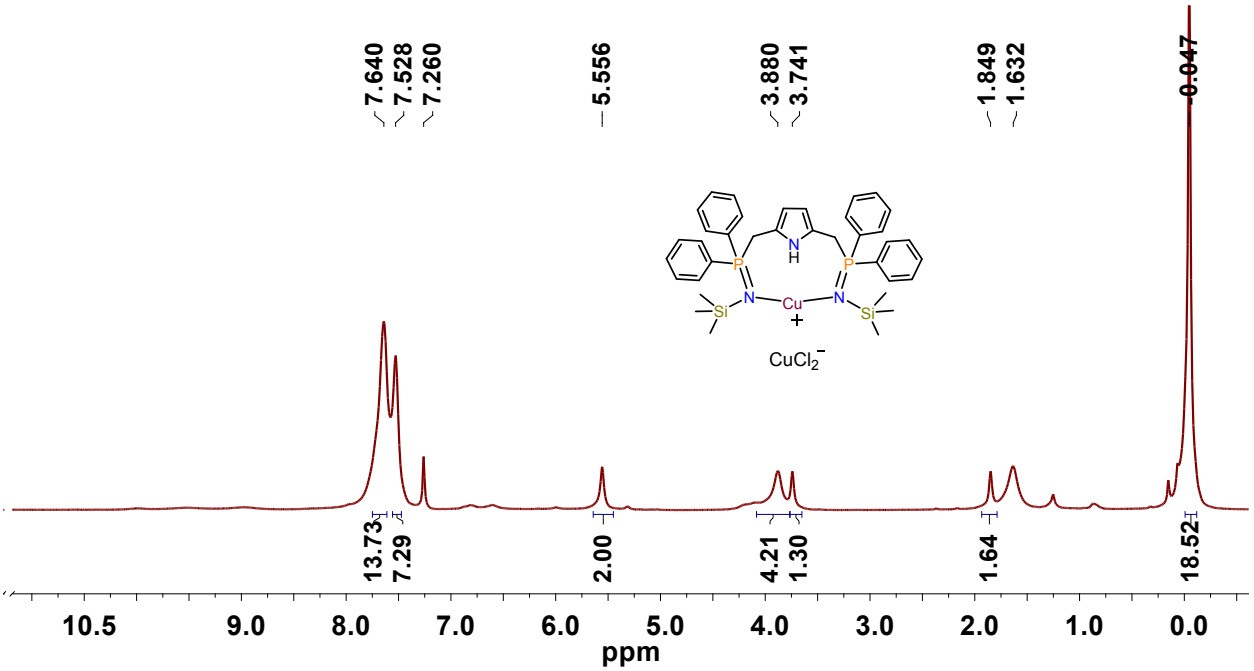

Figure S5. The ^{1}H NMR spectrum (600 MHz, 25 °C) of $[Cu\{C_4H_3N\text{-}2,5\text{-}(CH_2PPh_2NSiMe_3)_2\text{-}\kappa^2N,N\}]^+[CuCl_2]^-$ **3** in $CDCl_3$. Signals at δ 1.85 and 3.74 ppm are for THF as an impurity.

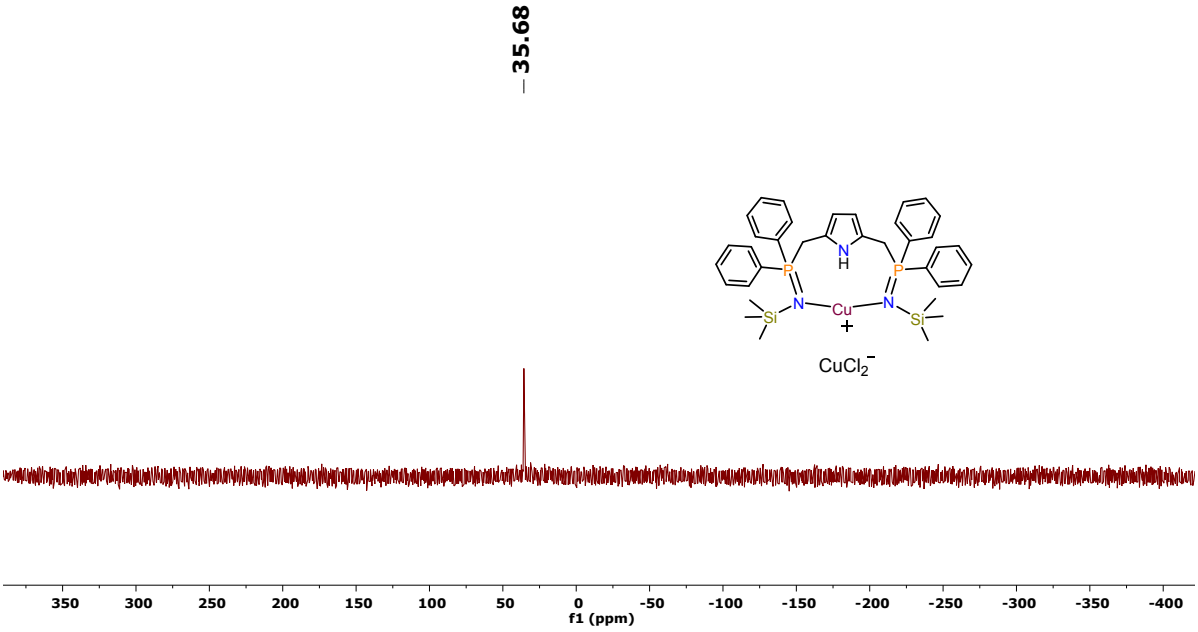

Figure S6. The $^{31}P\{^{1}H\}$ NMR spectrum (161.9 MHz, 25 °C) of **3** in $CDCl_3$.

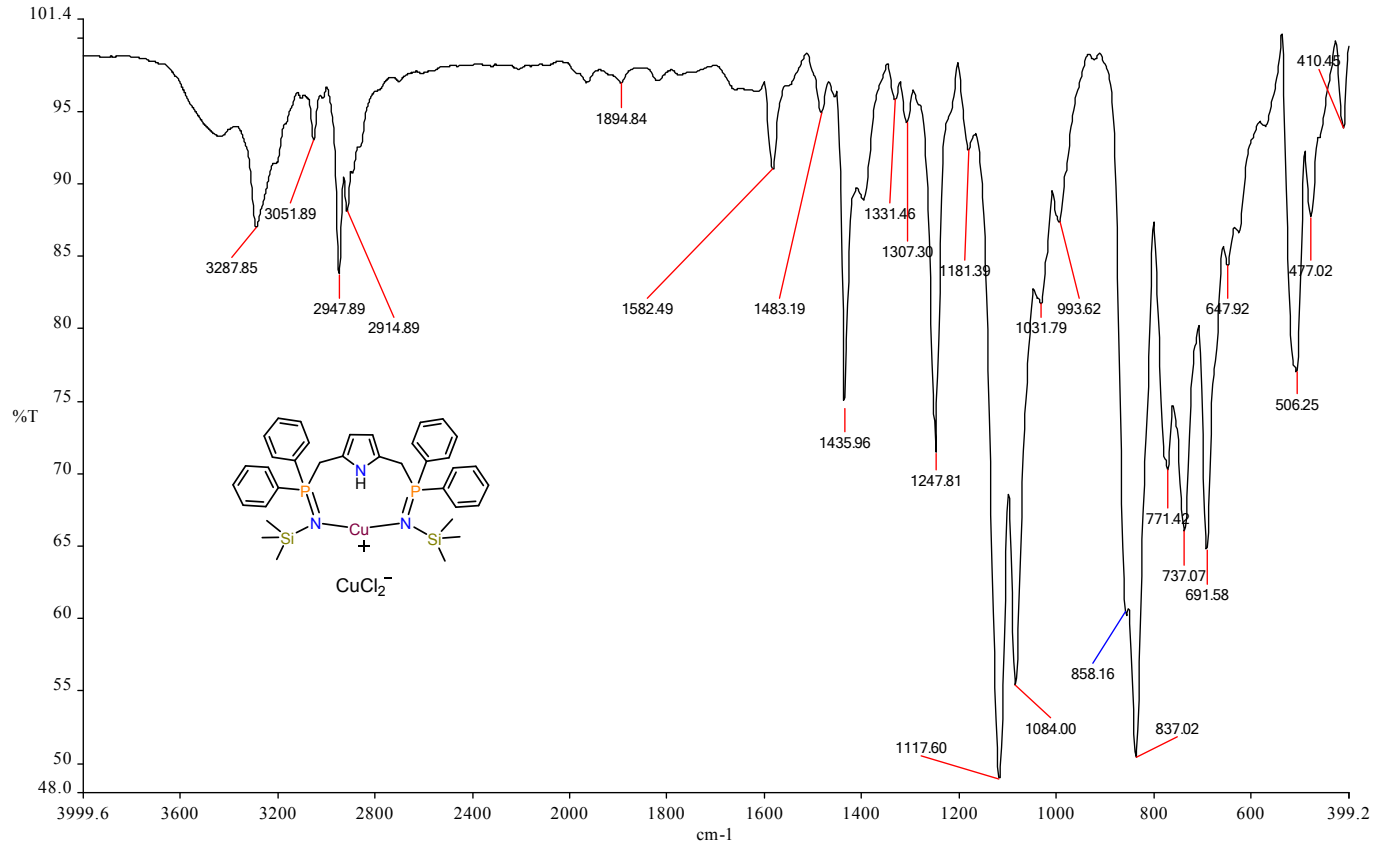

Figure S7. The FTIR spectrum of **3** recorded as a KBr disc.

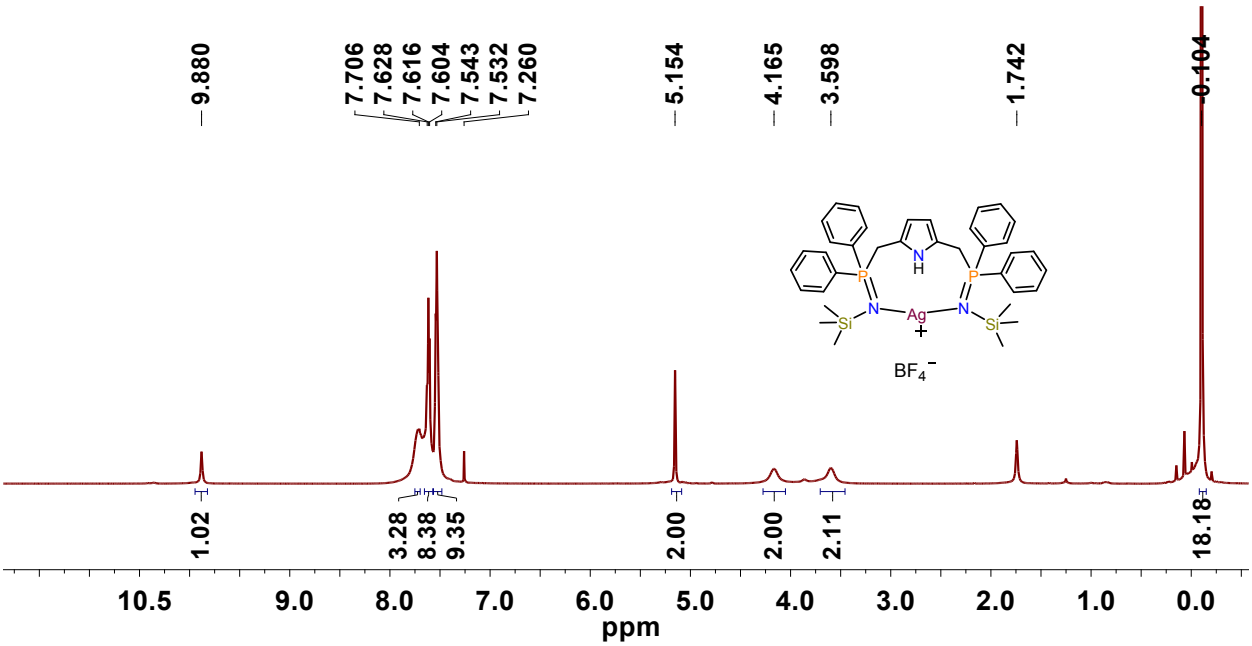

Figure S8. The ^{1}H NMR spectrum (600 MHz, 25 °C) of $[Ag\{C_4H_3N\text{-}2,5\text{-}(CH_2PPh_2NSiMe_3)_2\text{-}\kappa^2N,N\}]^+[BF_4]^-$ **4** in $CDCl_3$.

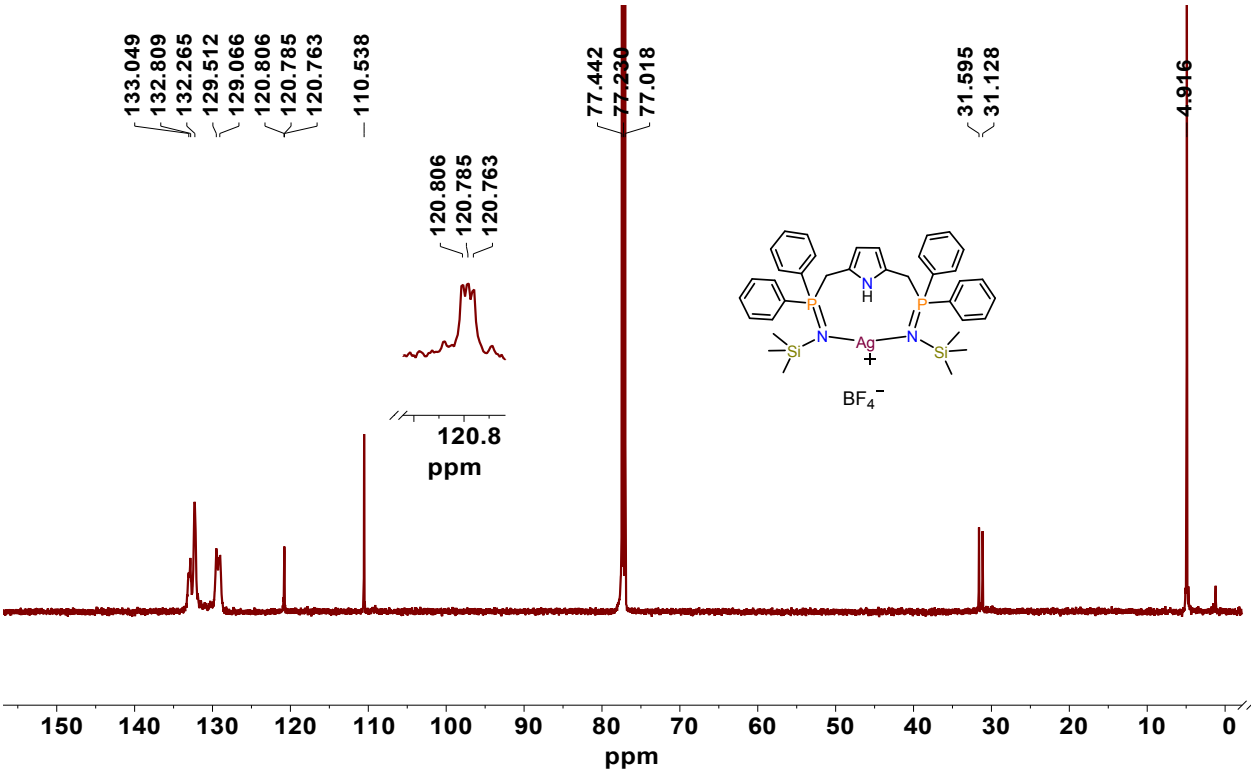

Figure S9. The ^{13}C NMR spectrum (150.9 MHz, 25 °C) of $[Ag\{C_4H_3N\text{-}2,5\text{-}(CH_2PPh_2NSiMe_3)_2\text{-}\kappa^2N,N\}]^+[BF_4]^-$ **4** in $CDCl_3$.

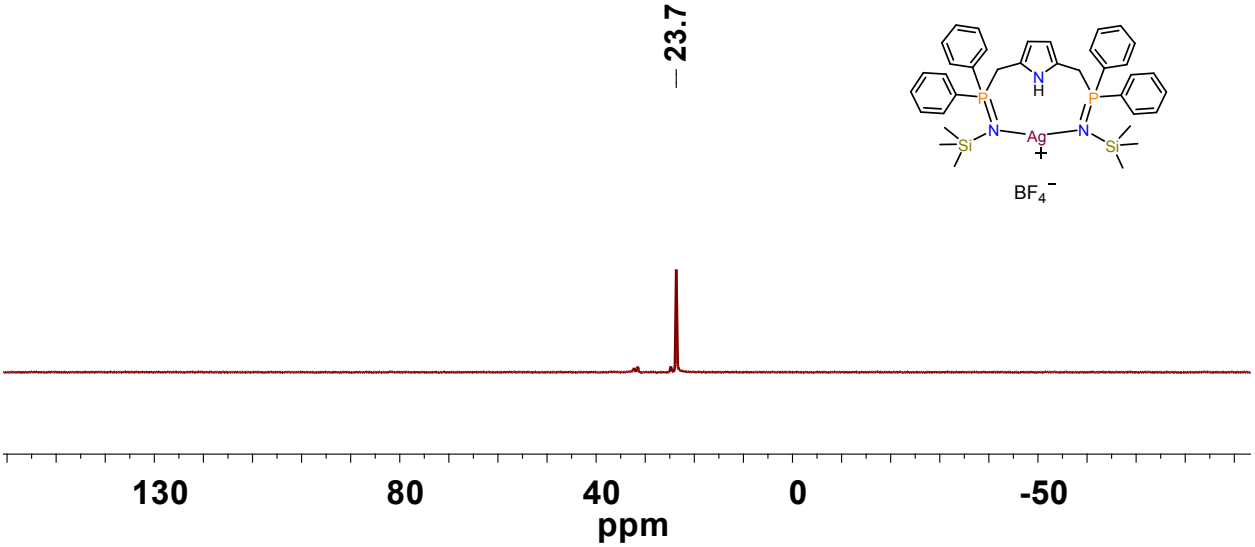

Figure S10. The $^{31}P\{^1H\}$ NMR spectrum (161.9 MHz, 25 °C) in $CDCl_3$ of $[Ag\{C_4H_3N\text{-}2,5\text{-}(CH_2PPh_2NSiMe_3)_2\text{-}\kappa^2N,N\}]^+[BF_4]^-$ **4** in $CDCl_3$.

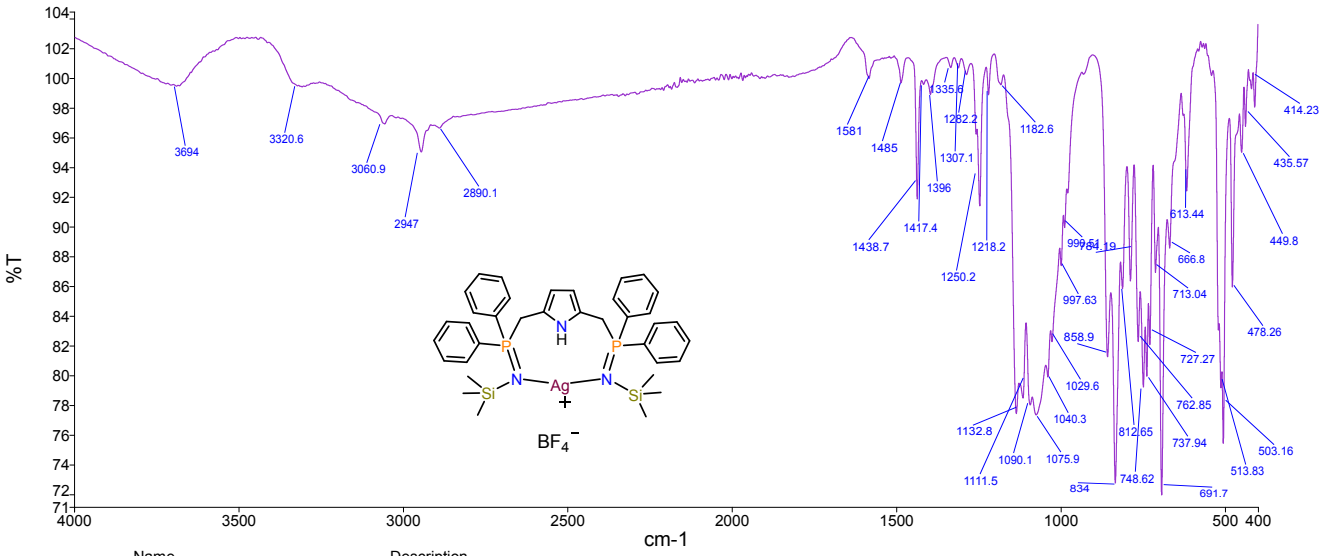

Figure S11. The FTIR spectrum (ATR mode) of [Ag{C_4H_3N-2,5-($CH_2PPh_2NSiMe_3$)$_2$-κ^2N,N}]$^+$[BF_4]$^-$ **4**.

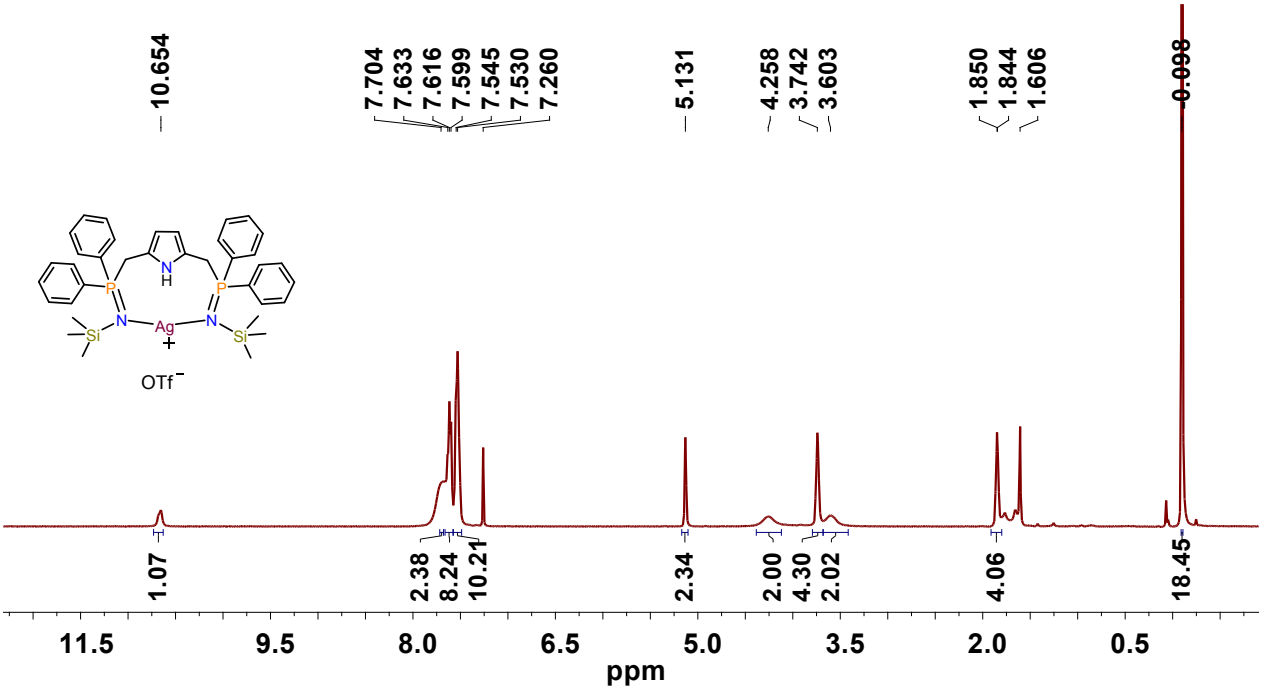

Figure S12. The ^{1}H NMR spectrum (600 MHz, 25 °C) of [Ag{C_4H_3N-2,5-($CH_2PPh_2NSiMe_3$)$_2$-κ^2N,N}]$^+$[OTf]$^-$ **5** in $CDCl_3$. Signals at δ 1.85 and 3.74 ppm are for THF present in the crystal lattice.

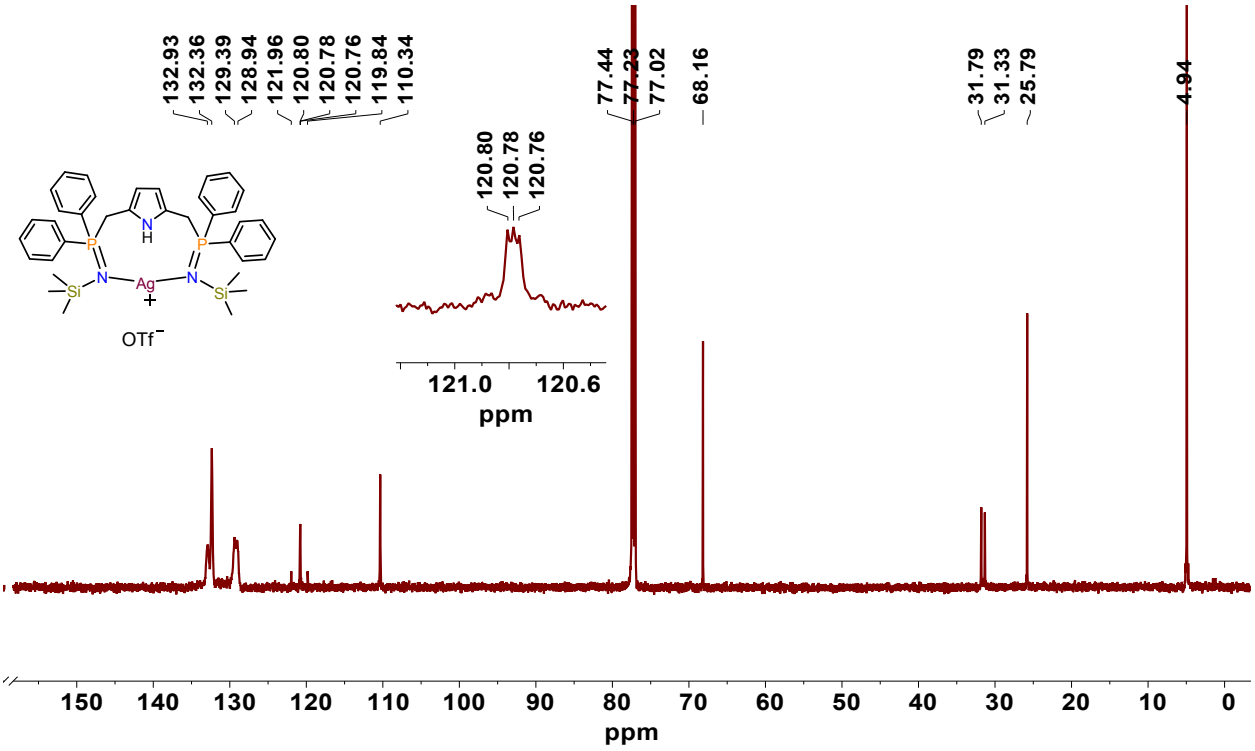

Figure S13. The ^{13}C NMR spectrum (150.9 MHz, 25 °C) of $[Ag\{C_4H_3N\text{-}2,5\text{-}(CH_2PPh_2NSiMe_3)_2\text{-}\kappa^2N,N\}]^+[OTf]^-$ **5** in $CDCl_3$. The signals at δ 25.8 and 68.2 are due to THF in the crystal lattice.

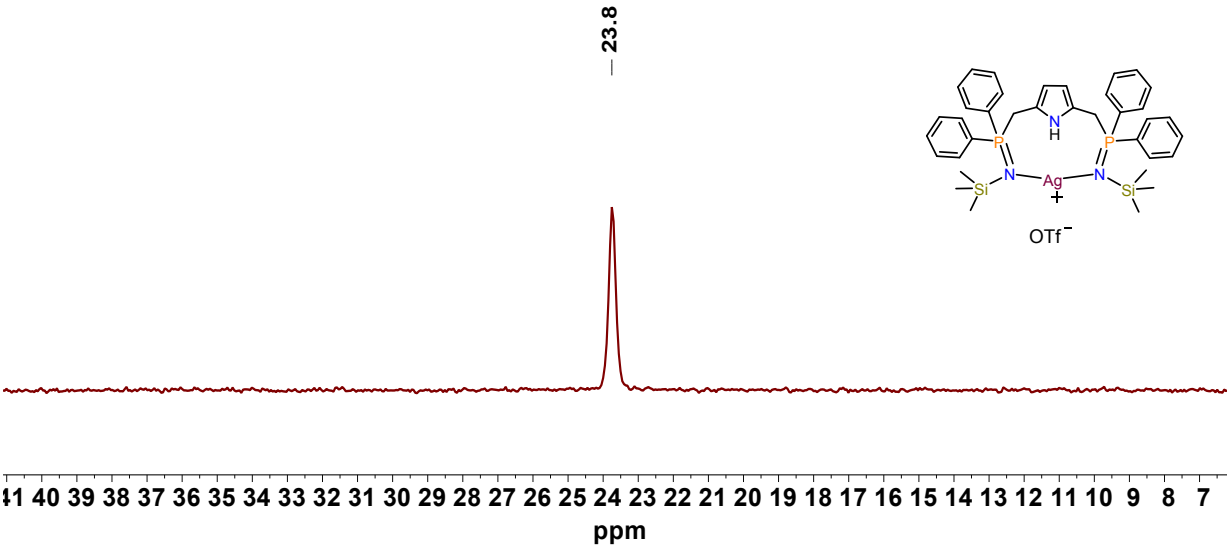

Figure S14. The $^{31}P\{^1H\}$ NMR spectrum (161.9 MHz, 25 °C) in $CDCl_3$ of $[Ag\{C_4H_3N\text{-}2,5\text{-}(CH_2PPh_2NSiMe_3)_2\text{-}\kappa^2N,N\}]^+[OTf]^-$, **5**.

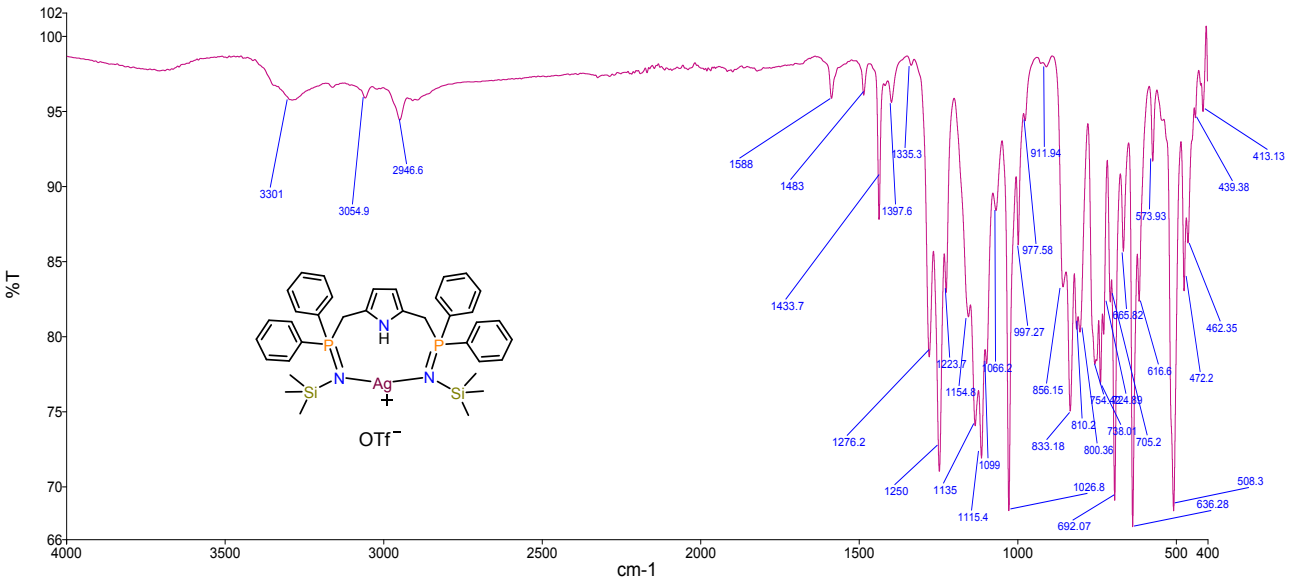

Figure S15. The FTIR spectrum (ATR mode) of $[Ag\{C_4H_3N\text{-}2,5\text{-}(CH_2PPh_2NSiMe_3)_2\text{-}\kappa^2N,N\}]^+[OTf]^-$ **5**.

X-ray crystallography

Table S1. The refinement data for structures **2**, **3**, **4** and **5**.

	2	**3**	**4**	**5**
Empirical formula	$C_{36}H_{45}N_3P_2Si_2$	$C_{36}H_{45}Cl_2Cu_2N_3P_2Si_2$	$C_{40}H_{53}AgBF_4N_3OP_2Si_2$	$C_{41}H_{53}AgF_3N_3O_4P_2SSi_2$
Formula weight	637.87	835.85	904.65	966.91
Wavelength (Å)	0.71073	0.71073	0.71073	0.71073
Temperature (K)	293(2)	100.15(2)	100.15(2)	100.15(2)
Crystal system	Orthorhombic	Triclinic	Triclinic	Triclinic
Space group	$C222_1$	$P\bar{1}$	$P\bar{1}$	$P\bar{1}$
a/Å	14.056(2)	12.3861(10)	10.9222(13)	10.9555(7)
b/Å	16.625(3)	12.8347(11)	13.9473(17)	14.0616(9)
c/Å	15.563(2)	13.8430(12)	15.3874(18)	15.4846(10)
α/degree	90	63.551(2)	104.166(4)	104.836(2)
β/degree	90	76.619(2)	105.854(3)	101.804(2)
γ/degree	90	83.611(2)	94.077(4)	92.257(2)
Volume (Å^3)	3636.8(10)	1916.7(3)	2162.3(4)	2246.5(3)
Z	4	2	2	2
D_{calcd}, g cm^{-3}	1.165	1.448	1.389	1.429
μ/mm^{-1}	0.213	1.425	0.647	0.675
F(000)	1360.0	864.0	936.0	1000.0
θ range (degree)	1.897 to 24.93	1.678 to 24.945	1.523 to 24.827	1.505 to 24.999
Limiting Indices	-16 ≤ h ≤ 16 -19 ≤ k ≤ 19 -17 ≤ l ≤ 18	−12 ≤ h ≤ 14 −15 ≤ k ≤ 15 −16 ≤ l ≤ 16	−12 ≤ h ≤ 12 −16 ≤ k ≤ 16 −18 ≤ l ≤ 18	−13 ≤ h ≤ 13 −16 ≤ k ≤ 15 −18 ≤ l ≤ 18
Total/ unique no. of reflns	21114/3161	22589/6647	25086/7344	26786/7871
R_{int}	0.0302	0.0350	0.0647	0.0731
Data/ restr./params.	3161/0/197	6647 / 64 / 432	7344/0/491	7871/0/518
GOF (F^2)	1.081	1.037	1.054	1.031
R1, wR2	0.0281, 0.0717	0.0423, 0.1114	0.0414, 0.0836	0.0507, 0.1060
R indices (all data) $R1$, $wR2$	0.0310, 0.0739	0.0516, 0.1175	0.0598, 0.0920	0.0805, 0.1177
Largest different peak and hole (e Å^{-3})	0.24, –0.12	1.58, –0.81	0.43, –0.57	0.88/–0.67

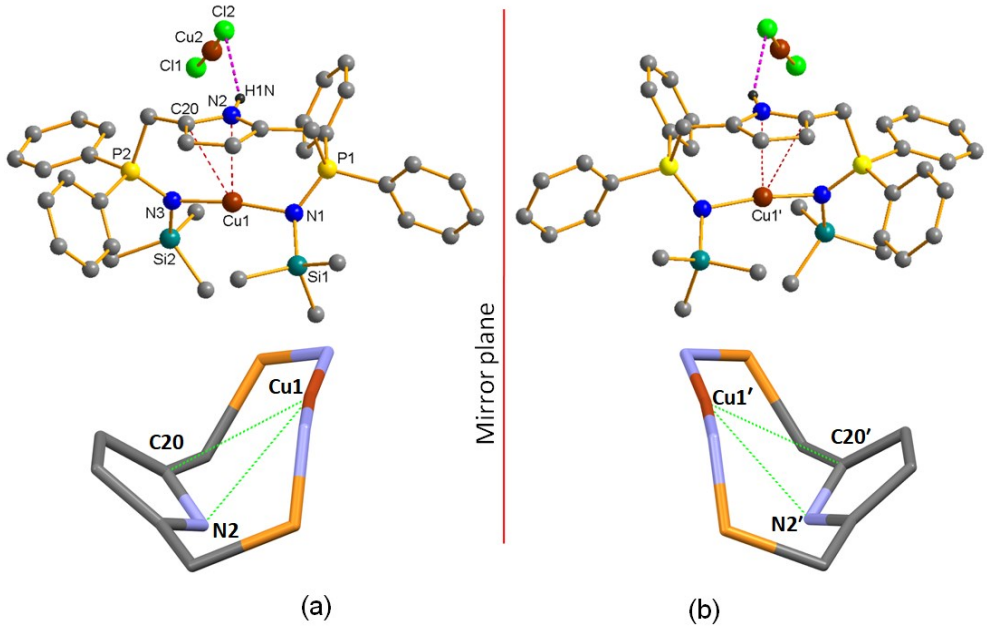

Figure S16. Enantiomers present in the crystal lattice of X-ray structure of complex **3**.

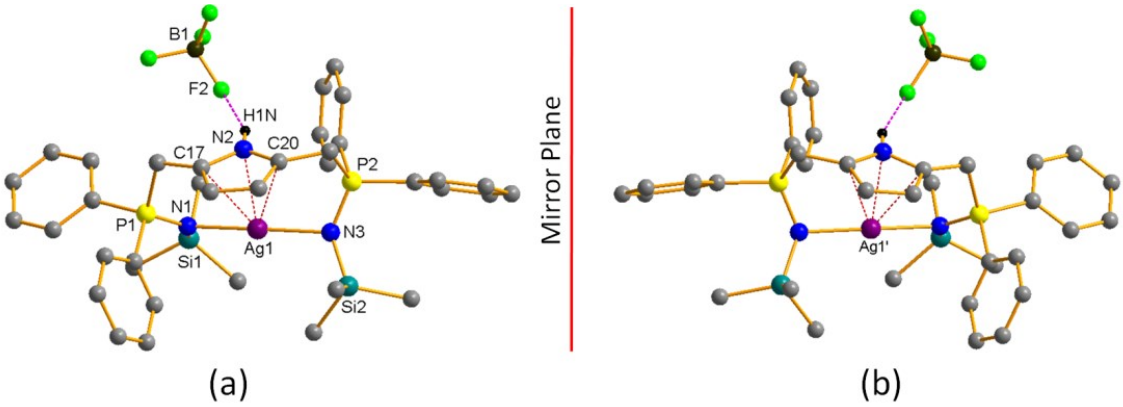

Figure S17. Enantiomers present in the crystal lattice of X-ray structure of complex **4**.

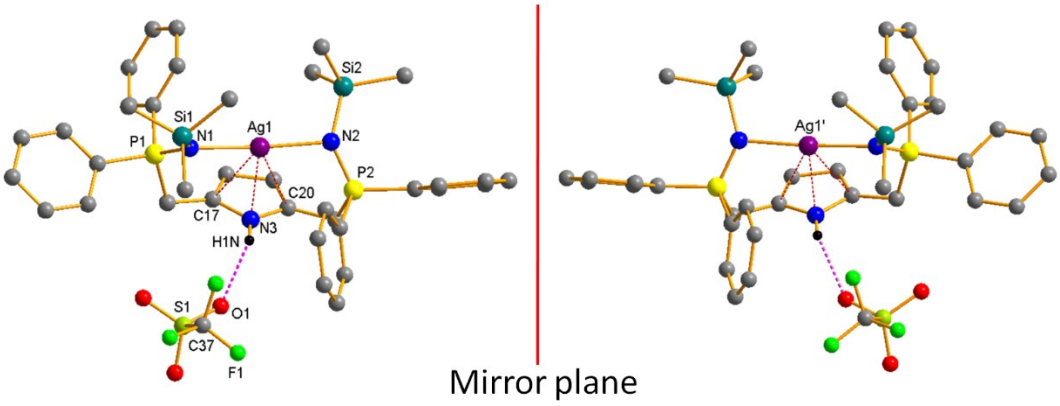

Figure S18. Enantiomers present in the crystal lattice of X-ray structure of complex **5**.

Table S2. Important bond distances in the free ligand **2** and its Cu(I) and Ag(I) complexes as obtained from the X-ray crystal structure and DFT optimization (wb97xd/Def2SVP). All distances in Å.

System	Si1-N1 Si2-N3 (imine)	P1-N1 P2-N3 (imine)	C_α-N2 (pyrrole)	M-N1 (imine)	M-N3 (imine)	M-N2 (pyrrole)	M-C_α	M-$C_{\alpha'}$
Ligand **2** (found)	1.682(2)	1.544(2)	1.363(3)					
Ligand **2** (Calc.)	1.717	1.557	1.366					
Complex **3** (found)	1.755(3), 1.792(6)	1.593(3), 1.598(3)	1.378(4), 1.369(4)	1.919(3)	1.905(3)	2.789(3)	3.217(3)	3.066(3)
Complex **3** (Calc.)	1.760, 1.769	1.600, 1.601	1.365, 1.367	1.944	1.917	2.837	3.222	3.001
Complex **4** (found)	1.731(3), 1.733(3)	1.587(3), 1.588(3)	1.382(4), 1.375(4)	2.143(3)	2.151(3)	2.809(3)	3.142(3)	3.193(4)
Complex **4** (Calc.)	1.768, 1.766	1.599, 1.598	1.374, 1.374	2.146	2.158	2.973	3.214	3.343
Complex **5** (found)	1.737(4) 1.738(4)	1.584(4), 1.584(4)	1.384(6), 1.378(6)	2.140(4)	2.153(4)	2.795(3)	3.117(4)	3.226(5)
Complex **5** (Calc.)	1.768, 1.767	1.599, 1.599	1.374, 1.375	2.146	2.159	2.974	3.216	3.343

Table S3. Mayer bond order in the free ligand **2** and its Cu(I) and Ag(I) complexes as obtained from their X-ray crystal structures and DFT optimization (wb97xd/Def2SVP).

Complex	Si1-N1 Si2-N3 (imine)	P1-N1 P2-N3 (imine)	C_α-N2 (pyrrole)
Ligand **2** (found)	1.1534	1.7012	1.2115
Ligand **2** (calc.)	1.0993	1.6697	1.2120
Complex **3** (found)	0.9164 0.8574	1.4068 1.3981	1.1815 1.1889
Complex **3** (calc.)	0.9291 0.8639	1.4014 1.3900	1.2031 1.2221
Complex **4** (found.)	0.9241 0.9306	1.4377 1.4588	1.1607 1.1478
Complex **4** (calc.)	0.9135 0.9121	1.4314 1.4484	1.1749 1.1731
Complex **5** (found)	0.9287 0.9265	1.4750 1.4376	1.1337 1.1584
Complex **5** (calc.)	0.9123 0.9146	1.4483 1.4314	1.1730 1.1749

Table S4. Bird aromaticity index of the pyrrole ring and the curvature of the electron density perpendicular to the pyrrole plane in the free ligand **2** and its Cu(I) and Ag(I) complexes.

Complex	Bird Aromaticity Index	Electron density curvature perpendicular to pyrrole plane
Ligand **2**	63.3	-2.0758
Complex **3**	60.8	0.1289
Complex **4**	59.5	3.3004
Complex **5**	59.1	8.7094

Table S5. Ligand strain energy in complex **3**, **4**, and **5**. The ligand strain energy is calculated from the difference in the energy of the ligand conformation in their crystal structures and its energy-optimized conformation.

Complex	Ligand strain energy (kcal/mol)	
	wb97xd/def2svp	B3LYP (with empirical dispersion)/def2svp
Complex **3**	25.1	24.0
Complex **4**	24.2	23.2
Complex **5**	24.3	23.2

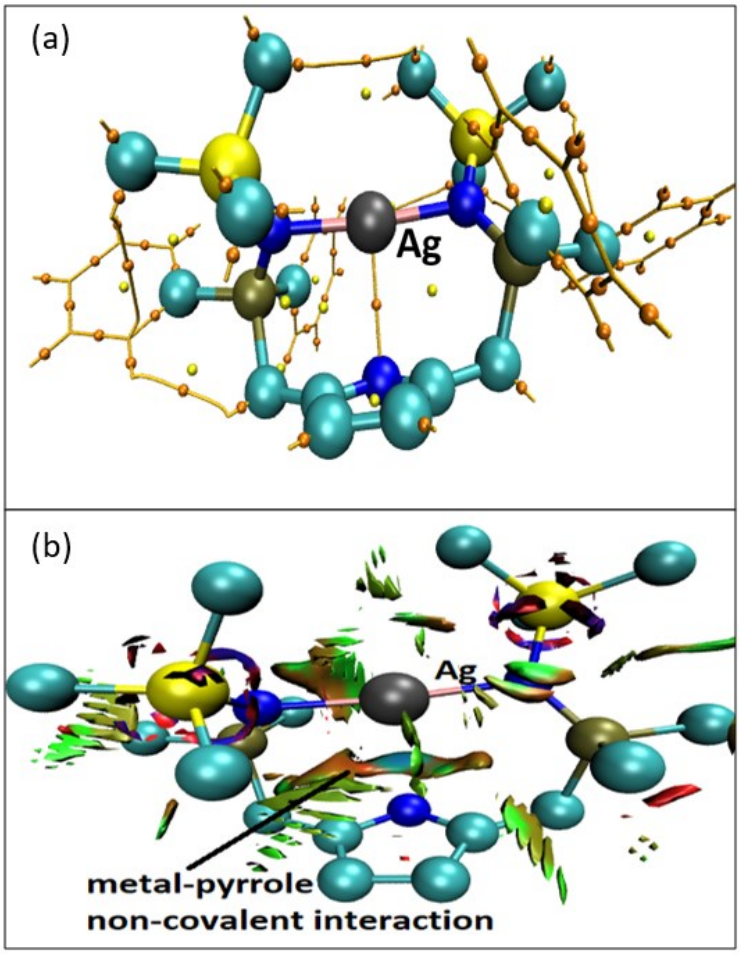

Figure S19. (a) The molecular graphs obtained from QTAIM and (b) the non-covalent interaction in silver(I) complex **4**. Hydrogen atoms and the phenyl groups are not shown for clarity. C, N, P, Si, and Ag are shown in cyan, blue, tan, yellow, and gray, respectively. The bond and ring critical points in (a) are shown in yellow and orange, respectively. A bond-critical point is found between the metal center and the N atom of pyrrole ring in (a). The isosurface between the metal ion and pyrrole ring in (b) indicates the metal-pyrrole non-covalent interactions (green surface indicates attractive interaction; brown surface indicates van der Waals interaction).

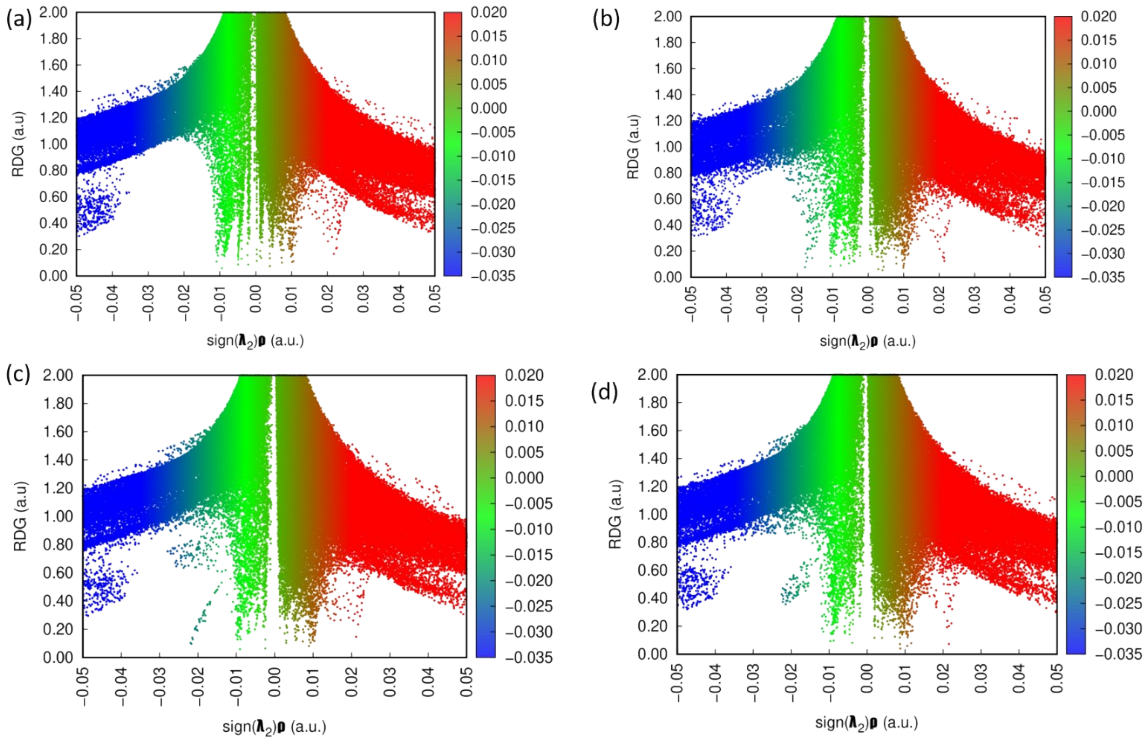

Figure S20. The color mapped scatter diagrams of non-covalent interactions in (a) metal free ligand **2**, (b) Cu(I) complex **3**, (c and d) Ag(I) complexes **4** and **5**. The y-axis shows the reduced density gradient and the x-axis shows the sign(λ2)ρ, where ρ represents the electron density and λ is the second largest eigenvalue of the electron density Hessian matrix. The blue and red colors reflect strong attractive (sign(λ_2)ρ <-0.01) and strong repulsive interactions (sign(λ_2)ρ>0.015), while the green indicates the weak interactions. The -0.01<sign(λ_2)ρ<0.0 regions represent the weak van der Waals interaction. Upon comparison of the plots for the metal free ligand and metal complexes, it can be seen that metalation has enhanced the weak non-covalent interactions in the complexes.

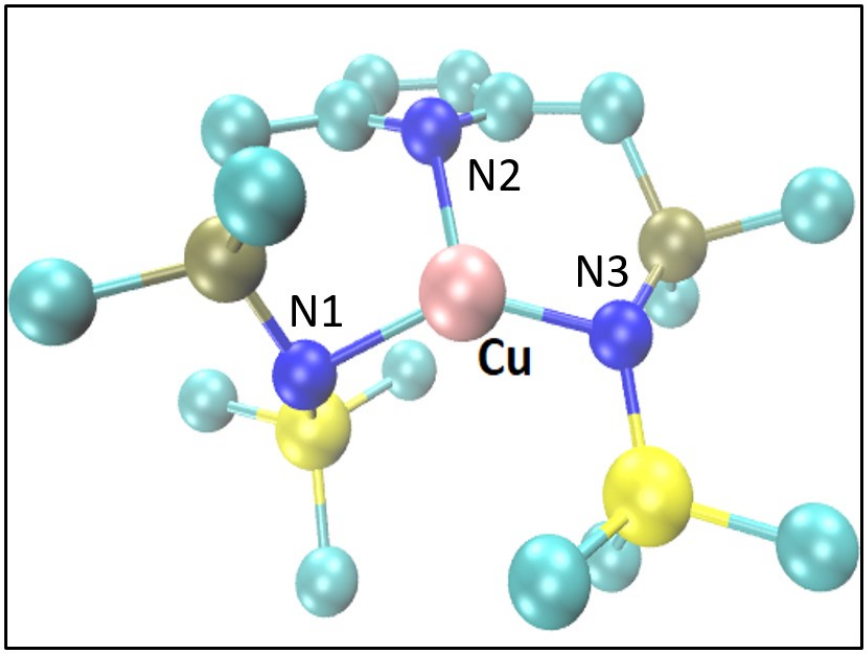

Figure S21. Optimized geometry of copper(I) complex containing the deprotonated form of ligand **2**. The Cu-N1(imine) = 2.01 Å, Cu-N2(pyrrole) = 2.05 Å, Cu-N3(imine) = 2.11 Å.